



Methane seepage dynamics and ground heating phenomena in the southern Po Valley: the case study of Santa Maria Nuova (Italy)

G. Capelli Ghioldi^{a,b,*}, G. Tamburello^b, A. Sciarra^c, D. Rouwet^b, T. Ricci^c , R. Civico^c, F. Tassi^a, P. Severi^d, M. Liuzzo^e, M. Coltorti^f, A.L. Rizzo^{g,h}

^a Department of Earth Sciences, University of Florence, Via G. La Pira 4, 50121, Firenze, Italy

^b INGV, Istituto Nazionale di Geofisica e Vulcanologia, Sezione di Bologna, Viale Bertini Pichat 6/2, 40127, Bologna, Italy

^c INGV, Istituto Nazionale di Geofisica e Vulcanologia, Sezione Roma 1, Via di Vigna Murata, 605, 00143, Rome, Italy

^d Geological, Soil and Seismic Area of the Emilia-Romagna Region, Viale Della Fiera 8, 40127, Bologna, Italy

^e INGV, Istituto Nazionale di Geofisica e Vulcanologia, Sezione di Palermo, Via Ugo La Malfa 153, 90146, Palermo, Italy

^f Department of Environmental Sciences and Prevention, University of Ferrara, Via Saragat 1, 44122, Ferrara, Italy

^g Department of Earth and Environmental Sciences, University of Milano-Bicocca, Milano, Italy

^h INGV, Istituto Nazionale di Geofisica e Vulcanologia, Sezione di Milano, Via Alfonso Corti, 12, 20133, Milano, Italy

ARTICLE INFO

Editorial handling by: Dr. Tao Wen

Keywords:

CH₄ seepage
Sedimentary basins
Microbial oxidation
Soil heating
Stable isotopes
RVI analysis

ABSTRACT

Natural reservoirs that release CH₄ can substantially increase atmospheric greenhouse gas levels, posing environmental and safety risks. Degassing phenomena in the Emilia-Romagna region (Italy) have been documented across a variety of fluids and reservoir types, with a focus on their origin and evolution. This study combines ground measurements and satellite data analysis to explore the relationships between CH₄ seepage, thermal anomalies, and vegetation stress at the Santa Maria Nuova (SMN) site in southern Po Valley. The explosion of a CH₄-saturated water well in July 2021 prompted a two-year investigation in the adjacent cultivated field (1.5 ha), revealing significant spatial and temporal variations in diffuse CH₄ fluxes (ranging from 0 to 917 g m⁻² d⁻¹) and corresponding CO₂ fluxes (1.9–466 g m⁻² d⁻¹). Soil temperature measurements and thermal imaging identified localised ground heating, attributed to methanotrophic exothermic oxidation of CH₄ to CO₂. These hotspots correspond to areas of visibly stressed vegetation, marked by reduced vitality and barren areas. Satellite-derived Ratio Vegetation Index (RVI) data confirmed persistent vegetation stress over the anomaly site from 2017 to 2024. Geochemical analysis of soil gases indicated a primarily biogenic origin of CH₄, supported by isotopic signatures ($\delta^{13}\text{C-CH}_4$ values < -60 ‰ V-PDB) and the presence of shallow Pleistocene carbonate deposits beneath the site, which can generate CH₄ seepage. These findings demonstrate the utility of integrating ground-based and remote sensing techniques for monitoring CH₄ seepage and its environmental impacts.

1. Introduction

Methane (CH₄) seepage refers to the release of natural gas from the subsurface into the surrounding environment. Methane-rich manifestations include onshore macro-seeps (such as mud volcanoes), submarine seepage, microseepage (as a diffusive flux from the soil), and thermal fluid discharges (Etioppe et al., 2007a, 2009; Ricci et al., 2023). Around 53 Tg CH₄ y⁻¹, nearly 10 % of the average global emission (EMEP/EEA, 2023), are emitted from natural gas reservoirs into the atmosphere. However, due to the spatial and temporal heterogeneity of emissions, these estimates carry considerable uncertainty, as they rely on either bottom-up approaches or top-down modelling. Consequently, they are

constrained by the extent of knowledge and the acquisition of direct measurements from geologically significant regions. A refined quantification of the geogenic CH₄ discharged into the atmosphere is crucial, as methane is a potent greenhouse gas with a global warming potential approximately 28–34 times higher than CO₂ over a 100-year period (IPCC et al., 2021). In addition to its role in climate change, atmospheric CH₄ affects tropospheric ozone formation and the oxidising capacity of the atmosphere. On a local scale, uncontrolled seepage of CH₄ and associated hydrocarbons may degrade air quality, alter soil microbial activity, and pose safety and environmental risks such as groundwater contamination and increased probability of explosions in confined spaces (Schout et al., 2020). Measurement of natural CH₄ emissions

* Corresponding author. Department of Earth Sciences, University of Florence, Via G. La Pira 4, 50121, Firenze, Italy.

E-mail address: gioia.capellighioldi@unifi.it (G. Capelli Ghioldi).

<https://doi.org/10.1016/j.apgeochem.2025.106565>

Received 24 February 2025; Received in revised form 29 July 2025; Accepted 9 September 2025

Available online 10 September 2025

0883-2927/© 2025 The Authors. Published by Elsevier Ltd. This is an open access article under the CC BY license (<http://creativecommons.org/licenses/by/4.0/>).

targets both diffusive degassing and punctual gas emissions, such as those from mud volcanoes and abandoned wells for hydrocarbon exploitation (e.g. Boothroyd et al., 2016).

Hydrocarbon-prone sedimentary basins host most macros and microseepages worldwide, which have long been used as indicators for potential oil or gas fields since the 1930s (Laubmeyer, 1933; Klusman, 1993; Tedesco, 1995; Abrams, 2005). In this environment, CH₄ is produced when organic matter buried within sediments undergoes biodegradation, carried out by microbial metabolic activity (biogenesis) and thermal alteration through cracking and reforming reactions caused by heat and pressure at depth (thermogenesis) (Schoell, 1980). Italy's methane reserves, currently totalling 37 billion cubic meters (ENI, 2023), result from Apennine orogenesis combined with Neogene tectonics and have been exploited for over a century, significantly reducing the surficial seepages (Etioppe, 2009). In the Emilia-Romagna region (north-central Italy), historical records documented the occurrence of unusual events in several areas, such as gas bubbling, abrupt temperature increases in well water, rapid changes in the level of aquifer table, soil deformation and temperature increase, soil liquefaction, and the formation of sand and mud volcanoes (Capaccioni et al., 2015; Bonzi et al., 2017; Ricci et al., 2023). These phenomena have been observed concurrently with earthquakes (e.g., Sciarra et al., 2012), although without a clear spatiotemporal correlation pattern, while they also characterise periods of seismic quiescence (Sciarra et al., 2017). Active tectonics in sectors under compressive regimes are closely related to these gas seeps, as they promote the upward migration of gas by increasing pore pressure or creating new fractures, thereby enhancing permeability (Klusman, 1993; Etioppe, 1999). Santa Maria Nuova Spallucci (hereafter referred to as SMN) is situated in the southeastern part of the Emilia-Romagna Region. In July 2021, a significant explosion was reported at this site, impacting a private water well. A spark from a water pump at the top of the well triggered the event. The rapid onset of a vigorous bubbling of CH₄-rich gases in the well water and a heavy metal panel at the well's exit created the conditions to rapidly exceed the lower flammability limit (4.4 vol% for CH₄) in the well and the subsequent explosion. During the survey in the following days, vigorous gas bubbling was still occurring, and non-dispersive infrared sensors placed at the wellhead revealed hazardous CH₄ levels (>5 vol%). The residents living in the neighbourhood reported the occurrence of numerous microseepage events over the last decades, such as gas bubbles in ponds on the ground during heavy rains or the interruption of construction work due to the presence of gas intercepted by excavations. Close to the well lies an agricultural field cultivated with barley, which displayed circular barren patches among the farming area. Similar surface manifestations have been observed in other areas of the region, such as the Terre Calde di Medolla (Modena province), where vegetative distress has been linked to diffuse gas emissions. In that area, CH₄ fluxes were found to drive methanotrophic oxidation, resulting in elevated CO₂ emissions and localised soil heating, ultimately causing persistent vegetation stress (Capaccioni et al., 2015; Sciarra et al., 2021). The explosion event, along with the presence of anomalous vegetation patterns in the adjacent field, prompted a detailed investigation of gas seepage dynamics at the SMN site, focusing on CH₄ and CO₂ emissions and the potential occurrence of processes analogous to those documented at the Medolla site. Specifically, the research aims to (i) quantify gas emissions employing ground-based measurements (i.e., accumulation chamber method), (ii) characterise the origin of these emissions in terms of depth and production processes, (iii) propose a method to identify potential sites where phenomena similar to those discussed in this paper may occur, by analysing satellite-derived vegetation data.

2. Study site

SMN is in the Romagna Plain, approximately 8 km from the boundary with the Northern Apennines (Fig. 1a). The ongoing evolution of the Northern Apennines into a fold-and-thrust belt since the

Cretaceous resulted from the collision between the European plate and the Adria microplate (Boccaletti et al., 1971; Marroni et al., 2002). Tectonic pressures arising from the reciprocal approach of the Alps and the Apennines, leading to a lowering in the central region, have generated the Po Valley. This vast subsiding area forms a sedimentary basin primarily filled with marine sediments at its deepest point. Alluvial sediments from rivers, including the Po River and its Alpine and Apennine tributaries, contributed to surface sedimentation through flooding (Severi and Bonzi, 2014). In the Emilia-Romagna plain, river-derived sediments are several hundred meters thick, overlaying coastal sediments and gradually transitioning to deeper and older marine deposits beneath. The geological units most affected by tectonic deformation are situated below those composing the deepest portion, buried by Plio-Pleistocene deposits (Capozzi and Picotti, 2002a). In the area including the study site, sandy-loamy alluvial deposits date back to the Roman and post-Roman periods (ISPRA, 2009), while in the subsurface, the alluvial deposits reach a depth of about 175 m (Emilia-Romagna Region-ENI Agip, 1998). The latter covers basal Middle Pleistocene coastal marine sediments, followed by progressively older marine deposits. SMN is roughly halfway between two buried thrust faults located near the Apennine margin (Fig. 1b) and a bundle of buried thrust faults positioned closer to the sea, while 1.5 km upstream from SMN, there is a normal fault. The contour lines of the Pliocene base demonstrate the presence of a complex tectonic framework. Active tectonic structures corresponding to buried thrust fronts are present in the subsurface. Near SMN, earthquakes with $4 < M_w < 5.5$ having hypocentres at about 8 km have been recorded (Fig. 1b). In the Apennine foothills near Forlì, biogenic CH₄ emissions occur within deformed upper Neogene foredeep deposits (Capozzi and Picotti, 2002b). These units constitute an uplifted segment of the primary hydrocarbon system exploited in the eastern Po Plain (Mattavelli et al., 1983). These seepages are linked to biogenic CH₄ produced by degradation of Pliocene and Pleistocene organic-rich layers. It is plausible that a transitional border exists between a deeply buried zone of organic matter responsible for thermogenic CH₄ production and a shallowly buried zone where bacteria can still ferment the organic matter in the foredeep succession (Capozzi and Picotti, 2010).

3. Materials and methods

3.1. Diffuse emissions of CH₄ and CO₂ from the soil and interstitial soil gases

Four seasonal field campaigns were conducted between May 2022 and October 2023 in the cultivated field at SMN to measure diffuse CH₄ and CO₂ fluxes from the soil. Flux measurements were carried out approximately every six months, and each survey was completed within a single day of fieldwork, providing a representative snapshot of emission patterns under different seasonal conditions. Sampling points were distributed across an area of approximately 1.5 ha, encompassing both zones with visible signs of vegetation stress and areas with normal vegetation cover. Locations with bare soil or sparse vegetation were generally easier to measure due to better surface accessibility. The spatial resolution varied between 75 and 130 measurement points per campaign, depending primarily on vegetation density and field accessibility. Gas flux measurements were carried out via the accumulation chamber method (Chiodini et al., 1998; Cardellini et al., 2003), using a portable West System™ flux meter equipped with a LICOR Li-820 infrared spectrophotometer for CO₂ and a tunable diode laser combined with a Herriott multipass cell for CH₄. The system operated with a Type B chamber, suitable for a wide range of fluxes. Measurement accuracy varies according to flux intensity: ±25 % for fluxes between 1 and 1500 mmol m⁻² d⁻¹, and ±10 % for fluxes between 1.5 and 300 mol m⁻² d⁻¹, as specified by the manufacturer. The measured fluxes (as g m⁻² d⁻¹) were processed through sequential Gaussian simulation (sGs) to extrapolate the values over a regular grid (5 × 5 m). The sGs geostatistical method mitigates the smoothing effects produced by

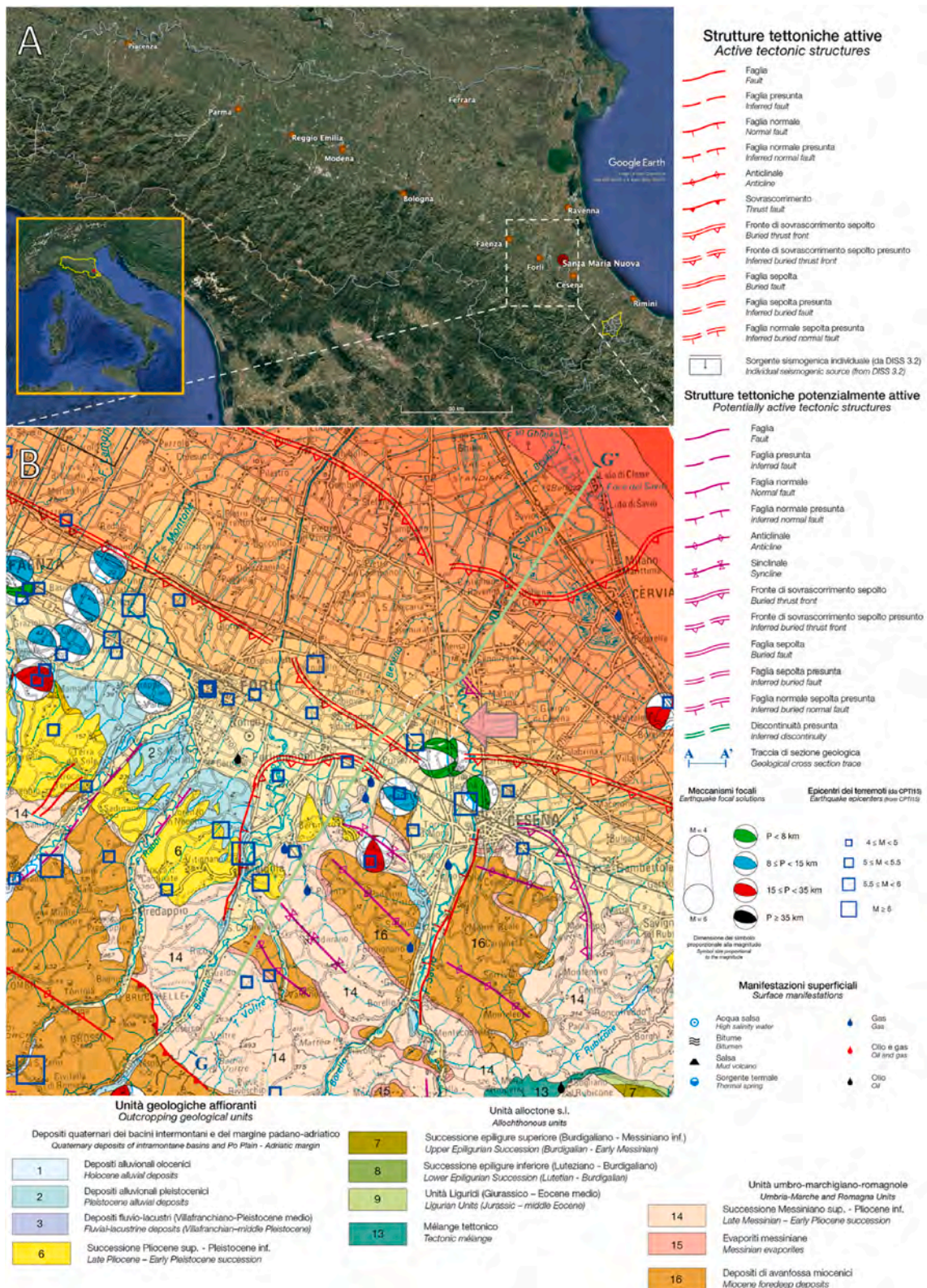


Fig. 1. Regional setting of the study area. (a) Satellite image of the Emilia-Romagna region (Google Earth) and its main cities, illustrating the location of the Santa Maria Nuova site (red circle). The grey dashed box corresponds to the detailed seismicotectonic map (b), which displays the primary tectonic structures and geological formations in the vicinity of SMN (indicated by the pink arrow and encircled in white), the locations of earthquakes along with their magnitude and depth, as well as reports of hydrocarbon manifestations, including a trace of geological cross-section G-G' (highlighted in green) that passes over the site. To view the complete map, please consult https://mappegis.regione.emilia-romagna.it/gstatico/documenti/sismotett_2016/Carta_Sismotettonica.pdf. (For interpretation of the references to colour in this figure legend, the reader is referred to the Web version of this article.)

deterministic methods (e.g., ordinary Kriging) by generating multiple random realisations. In sGs, during the estimating procedure for each unknown point, both the estimates at the previously simulated sites and the actual values at sampled locations are considered (Deutsch and Journel, 1998). For every dataset, 200 simulations were produced and post-processed to construct CH₄ and CO₂ flux maps. The total output in t d⁻¹ was computed based on the integration of the extrapolated fluxes over the entire area. Interstitial gas samples were collected where the gas flux and soil temperatures were anomalous (Fig. 2a). According to Tassi et al. (2015), soil gas was collected using a stainless-steel tube with

an inner diameter of 4 mm at approximately 25 cm depth inserted into the soil and connected to a 100 mL syringe via a PTFE three-way valve used to fill a 1L air sampling bags (Supelco®). Both inorganic (O₂, N₂, CO₂) and organic (CH₄) gases were analysed at the Fluid Geochemistry Laboratory of INGV Rome by a MicroGC Varian 4900, with an analytical error <3 %. The isotopic carbon ratio of both CO₂ and CH₄ (expressed as δ¹³C-CO₂ and δ¹³C-CH₄, Vienna PeeDee Belemnite (VPDB) ‰) was determined via cavity ringdown spectroscopy (CDRS) with the Picarro G2201-i instrument, with a precision within 0.16 ‰ for δ¹³C-CO₂ and 1.15 ‰ for δ¹³C-CH₄.



Fig. 2. (a) Aerial view of the SMN field and surrounding area. The yellow dashed line outlines the cultivated field where gas flux measurements were conducted. The red circle shows the location of the CH₄ saturated well, and orange triangles indicate the sampling points for interstitial gas. (b) A time series of satellite photographs (Google Earth) of the field emphasizing the persistence of the anomaly in the vegetation. (For interpretation of the references to colour in this figure legend, the reader is referred to the Web version of this article.)

3.2. Soil temperatures

To detect and characterise near-surface thermal anomalies potentially related to gas seepage, a multi-scale thermal survey was carried out. The September 2022 flux campaign was preceded by a drone-based thermal imaging survey using a DJI Matrice 300 UAV, equipped with a Zenmuse H20T radiometric thermal sensor, flown at 60 m above ground level. From that survey onward, each flux measurement campaign involved collecting soil temperature data at a depth of approximately 10 cm using a digital thermometer with a Type-K thermocouple of 20 cm. Thermal maps were also generated using the sGs method. Additionally, in 2024, a soil temperature station equipped with a Mini T1 datalogger and thermocouple was installed at the main anomaly spot at a depth of about 50 cm, from January to November. This dataset is included in the Supplementary Material (Fig. S1).

3.3. Vegetative cover and Sentinel-2 spectral data processing

After screening the area with Google Earth Pro to assess the temporal persistence of vegetation anomalies (Fig. 2b), these features were interpreted as a spatial indicator of CH₄ seepage in the field. The presence of a recurrent vegetation stress signal over several years supported its use as a preliminary guide for field investigations. These associations between plant stress, ground heating, and natural gas emissions, already demonstrated in the Terre Calde di Medolla site (Capaccioni et al., 2015; Sciarra et al., 2021), further strengthened their role as reliable indicators of subsurface gas migration. To corroborate the observations from the analysis of the satellite images, the cloud-based platform for geospatial analysis, Google Earth Engine (GEE, <https://earthengine.google.com/>), provided an extensive database of satellite acquisitions that enabled spectral data processing. Specifically, the distinct spectral conditions of various vegetative covers can be identified by their overall ground elements: while leaf cellular structures strongly reflect near-infrared radiation (760–900 nm), visible radiation in the red (630–690 nm) is absorbed by chlorophyll (Tucker, 1979). Combining these two spectral domains makes it possible to distinguish plants from the soil and use vegetative cover density to calculate photosynthetically active biomass. The “Ratio Vegetation Index” (RVI), developed by Pearson and Miller (1972), enhances the contrast between the ground and vegetation:

$$RVI = \frac{NIR - R}{NIR + R} \quad (1)$$

Where R is the mean reflectance in the red channel, and NIR is the mean reflectance in the near-infrared channel. Considering this, the temporal trend of plant growth inhibition associated with gas seepage was evaluated by calculating the RVI of two different circular areas (~30 m radius) in the field: (1) one located in the central zone of the vegetative anomaly, where the ground was consistently bare or sparsely vegetated (RVI_{an}) and (2) one in a reference area with nominally healthy vegetation, used as background (RVI_{bg}). The selection of these areas was guided by the CH₄ flux maps obtained during the initial field campaigns, which helped to delineate zones of active seepage and unaffected vegetation. The Sentinel-2 spatial resolution for both spectral bands was 10 m, and the RVI was calculated considering the cloud coverage probability and excluding all R band values < 0.1, i.e. the cloud threshold value proposed by the sentinel2-cloud-detector library.

3.4. Groundwater monitoring at the exploded well

The exploded water well was equipped with an STS DL.WMS.BT.4G. LTC multi-parameter probe to continuously monitor potential signals of deep fluid migration. The probe includes a pressure sensor (0.05 % full-scale accuracy), a temperature sensor (± 0.1 °C), and a four-electrode electrical conductivity sensor with six titanium electrodes and a measurement error below 2.5 % of the range. Data were recorded at hourly intervals. The time series collected between June 2023 and December

2024 is presented and discussed in the Supplementary Material (Fig. S2).

4. Results

4.1. Diffuse gas emissions from the SMN field

Table 1 presents a statistical summary of CH₄ and CO₂ fluxes from the soil, along with the output estimates obtained from the sGs extrapolation, during the 2022–2023 campaigns. In May 2022, Φ_{CH_4} varied from 0 to 917 g m⁻² d⁻¹, yielding a total estimated output of 0.82 ± 0.1 t d⁻¹. Φ_{CO_2} fluctuated between 28.2 and 308.5 g m⁻² d⁻¹, leading to a total emission of 1.8 ± 0.18 t d⁻¹. By September 2022, CH₄ fluxes had significantly decreased, with values ranging from 0 to 5.8 g m⁻² d⁻¹ and a total output of 0.008 ± 0.003 t d⁻¹, while Φ_{CO_2} spanned from 9.4 to 174.8 g m⁻² d⁻¹, with an output of 0.62 ± 0.05 t d⁻¹. The April 2023 campaign showed a new peak for CH₄, with fluxes up to 224.4 g m⁻² d⁻¹ and an estimated total output of 0.51 ± 0.09 t d⁻¹, whereas CO₂ fluxes ranged from 5.2 to 157.8 g m⁻² d⁻¹, contributing to a total emission of 0.65 ± 0.07 t d⁻¹. Finally, in October 2023, CH₄ fluxes were once again low, ranging from 0 to 4.6 g m⁻² d⁻¹, with a total output of 0.005 ± 0.002 t d⁻¹. CO₂ fluxes exhibited a broader range, from 1.9 to 466.1 g m⁻² d⁻¹, with an overall emission of 0.66 ± 0.04 t d⁻¹. The spatial distributions of CH₄ and CO₂ fluxes, as derived from sGs interpolation, are shown in Fig. 3, where a permanent anomaly can be observed, particularly to the south of the agricultural field, throughout the two-year monitoring period.

4.2. Interstitial soil gases and isotopic data

The analytical results for interstitial gases collected in September 2022 and April 2023 are summarised in Table 2. CH₄ concentrations ranged from 0.00074 % (22A) to 54.1 % (23E), while CO₂ concentrations ranged from 0.07 % (23A) to 6.88 % (23D). The CH₄/CO₂ molar ratio spanned from 0.01 (22A) to 8.80 (23C), whereas O₂ content ranged between 4.7 % (22B) to 20.03 % (23F), and N₂ values varied from 37.6 % (23E) to 78.7 % (23A). The $\delta^{13}C$ values in CH₄ ranged from -61 ‰ V-PDB (22A) to -77.8 ‰ V-PDB (23E), while the $\delta^{13}C$ -CO₂ values were from -52 ‰ V-PDB (23D) to -24 ‰ V-PDB (23C). These data are graphically represented in Fig. 4, where panel (a) reports the $\delta^{13}C$ values of CH₄ and CO₂ for all samples, and panel (b) shows the CH₄/CO₂ molar ratio plotted against $\delta^{13}C$ -CO₂.

Table 1

Descriptive statistics of the soil diffuse CH₄ and CO₂ flux values for the 2022–2023 surveys (in g m⁻² d⁻¹) and total output in t d⁻¹.

	Φ_{CH_4} (g m ⁻² d ⁻¹)				
	Value Range	Mean	Median	Standard Deviation	Output in t d ⁻¹
May 2022	0–916.9	25.3	11.6	51.3	0.82 ± 0.1
September 2022	0–5.8	0.5	0.4	0.4	0.008 ± 0.003
April 2023	0–224.4	28.2	18.1	31.7	0.51 ± 0.09
October 2023	0–4.6	0.4	0.2	0.5	0.005 ± 0.002
	Φ_{CO_2} (g m ⁻² d ⁻¹)				
	Value Range	Mean	Median	Standard Deviation	Output in t d ⁻¹
May 2022	28.2–308.5	73.8	63.8	35.8	1.8 ± 0.18
September 2022	9.4–174.8	42.4	35.8	24.3	0.62 ± 0.05
April 2023	5.2–157.8	37.2	31.7	24.2	0.65 ± 0.07
October 2023	1.9–466.1	43.9	26.3	48.3	0.66 ± 0.04

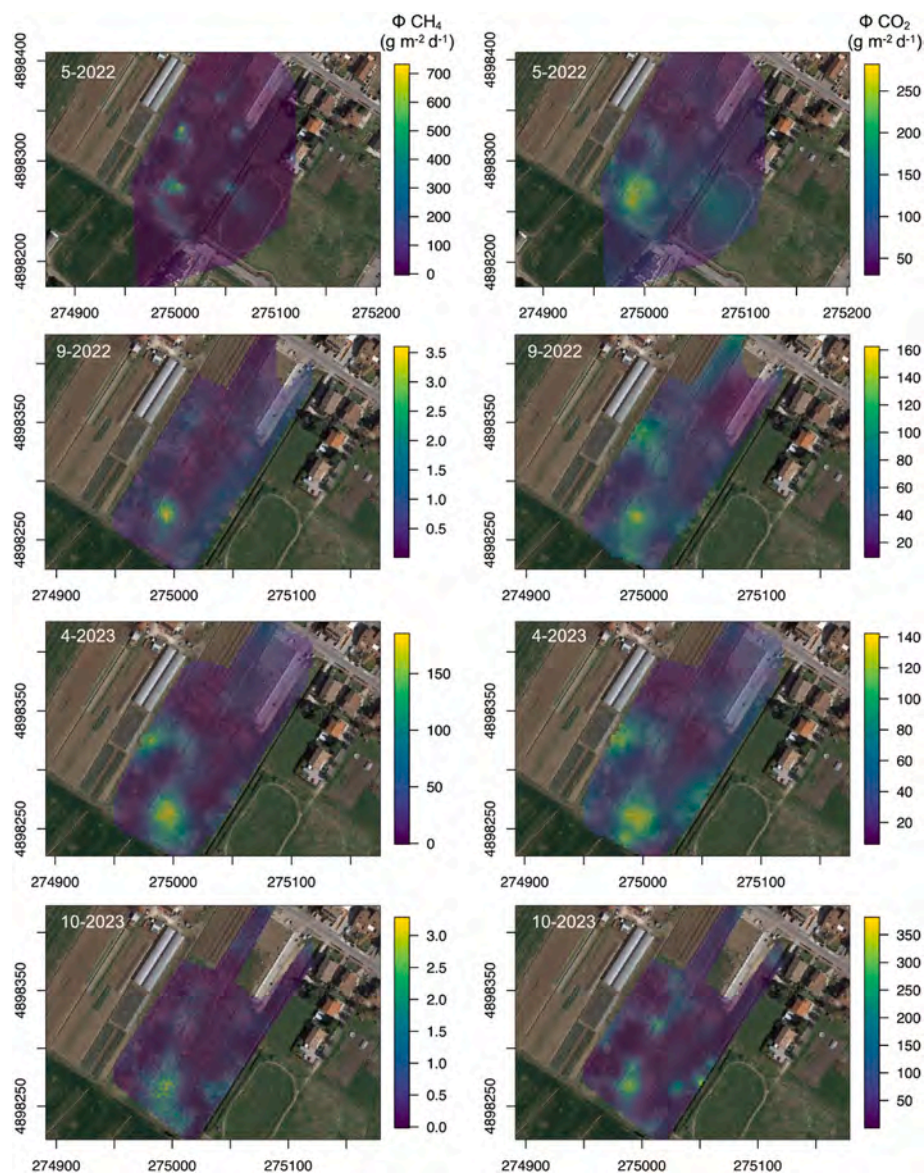


Fig. 3. Flux distribution of CH₄ and CO₂ at the SMN Site during the 2022–2023 observation period. Both flux measurements were processed using a Sequential Gaussian Simulation and are expressed in g m⁻² d⁻¹.

Table 2

Displays the sample ID, date, depth, chemical composition in vol%, and the CH₄/CO₂ ratio, along with the isotopic carbon ratios of CO₂ and CH₄ expressed as δ¹³C‰V-PDB for the interstitial gases at the SMN field. The analysis for sample 23A* relates to a slightly greater depth of 35 cm.

ID	Date	O ₂ vol %	N ₂ vol %	CH ₄ vol %	CO ₂ vol %	CH ₄ /CO ₂	δ ¹³ C–CH ₄ ‰ V-PDB	δ ¹³ C–CO ₂ ‰ V-PDB
22A	2022/09/23	19.7	75.5	0.00074	0.09	0.01	–61	–25
22B	2022/09/23	4.7	61.7	29.78	6.43	4.63	–74.5	–30
23A	2023/04/04	19.99	78.71	0.95	0.07	13.57	–72	–26
23A*	2023/04/04	19.99	77.65	1.03	0.09	11.44	–68	–39
23B	2023/04/04	17.73	72.57	7.05	1.23	5.73	–69	–35
23C	2023/04/04	17.74	72.14	7.74	0.88	8.8	–76	–24
23D	2023/04/04	8.25	59.29	25.57	6.88	3.72	–68	–52
23E	2023/04/04	6.07	37.61	54.08	2.69	20.1	–77.8	–37
23F	2023/04/04	20.03	78.32	0.01	0.15	0.07	–72	–

4.3. Soil temperature measurements

The spatial distribution of ground surface temperatures obtained through both UAV-based thermal imaging and point-based measurements during the flux campaigns is shown in Fig. 5. Panel (a) shows the

thermal orthomosaic acquired via drone prior to the September 2022 campaign. A warmer area is clearly visible in the southern-central sector of the cultivated field, where surface temperatures exceed 17 °C, contrasting with surrounding zones measuring as low as ~3 °C. Panels (b), (c), and (d) display soil temperature data collected at ~10 cm depth

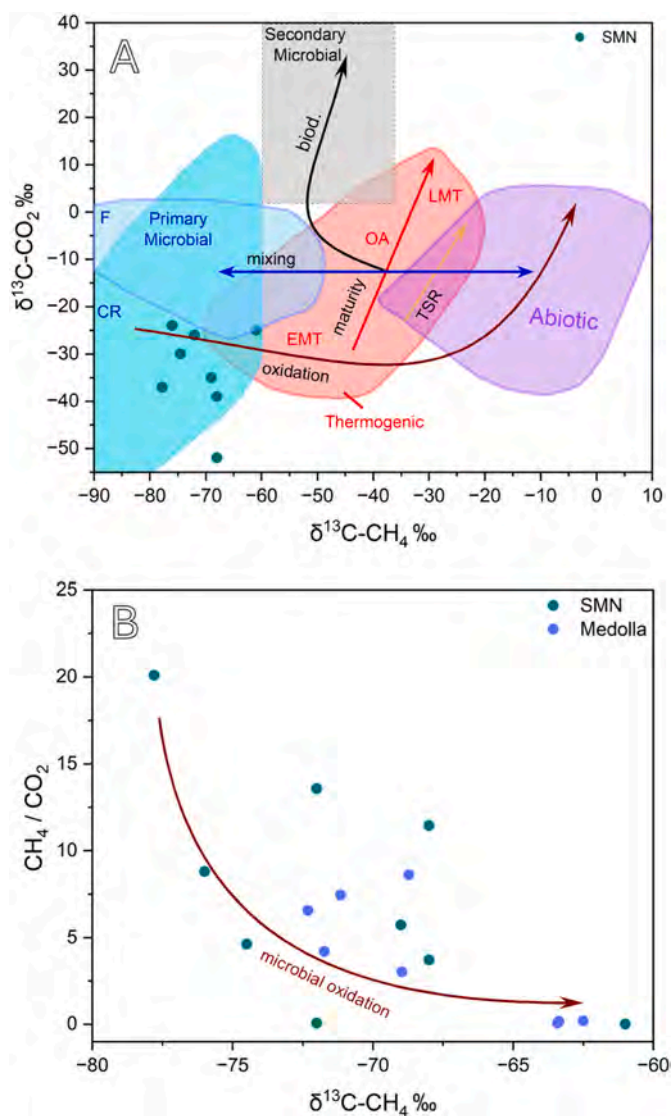


Fig. 4. (a) SMN soil gas samples are plotted on a diagram of $\delta^{13}\text{C}-\text{CH}_4$ versus $\delta^{13}\text{C}-\text{CO}_2$, which includes genetic fields and processes influencing the carbon isotopic composition of CH_4 and CO_2 in natural gases, as proposed by Milkov and Etiope (2018). Field acronyms denote CO_2 reduction (CR), methyl-type fermentation (F), secondary microbial (SM), early mature thermogenic gas (EMT), oil-associated thermogenic gas (OA), and late mature thermogenic gas (LMT); while process acronyms represent biodegradation (biodeg.) and thermochemical sulphate reduction (TSR). (b) Binary diagram of $\delta^{13}\text{C}-\text{CH}_4$ versus CH_4/CO_2 ratio for the SMN soil gas samples (green) and the Terre Calde di Medolla soil gas samples (cyan) taken from Capaccioni et al. (2015). (For interpretation of the references to colour in this figure legend, the reader is referred to the Web version of this article.)

during the surveys conducted in September 2022, April 2023, and October 2023, respectively. In all three cases, a consistent temperature gradient is observed across the field, with relatively higher values located in the central-southern portion where vegetation appears sparser or absent. The temperature difference between warmer and cooler zones varies across the three campaigns: approximately 5 °C in September 2022 (panel b), up to 3.5 °C in April 2023 (panel c), and exceeding 10 °C in October 2023 (panel d). The more pronounced contrast visible in the UAV-derived dataset (panel a) is further addressed in the Discussion section.

4.4. RVI analysis

The temporal evolution of the RVI calculated from Sentinel-2 satellite data for both the SMN and Medolla fields is shown in Fig. 6. The Medolla site is included in the analysis as it represents another location where vegetation stress has been documented in association with similar phenomena. At the Medolla site, the RVI_{an} was calculated over a larger anomaly area rather than a single point, capturing a broader spatial impact. Both graphs cover the period from July 2017 to May 2024. At the SMN site (upper panel), RVI_{bg} values (green circles) exhibit a clear seasonal pattern, with sharp increases during the spring and early summer of each year. These peaks vary in magnitude, with particularly high values recorded in 2019 and again between 2022 and 2023. Notably, RVI_{bg} values show greater dispersion and variability compared to the RVI_{an} values. The RVI_{an} data (orange squares) display a lower amplitude of seasonal variation throughout the time series, with most values remaining below 4. The contrast between RVI_{an} and RVI_{bg} is especially marked during the peak growing seasons, when RVI_{bg} reaches its highest values, while RVI_{an} remains comparatively stable or only moderately increases. Dashed vertical lines indicate the four time points corresponding to the flux campaigns conducted in May 2022, September 2022, April 2023, and October 2023. At the Medolla site (lower panel), both RVI_{bg} and RVI_{an} show well-defined seasonal cycles, with elevated values during vegetative periods and lower values during the winter months. As at SMN, RVI_{bg} generally displays higher peaks than the corresponding RVI_{an} , although the two curves follow a more similar trend over time compared to SMN. Peak RVI_{bg} values often exceed 15 and reach up to ~25–27 in some years (notably in 2019 and 2020), whereas RVI_{an} values mostly remain below 15, even during peak growing seasons.

5. Discussion

5.1. Origin of gases

Methane in natural environments is mainly produced by two genetic processes, which can be distinguished using the carbon isotopic ratio of CH_4 , expressed as $\delta^{13}\text{C}-\text{CH}_4$. Biogenic CH_4 , mostly related to microbial activity in anoxic conditions, typically exhibits strongly depleted $\delta^{13}\text{C}$ values < -50 ‰ V-PDB, whereas thermogenic CH_4 , formed from the thermal decomposition of organic matter at high temperatures, shows less negative $\delta^{13}\text{C}$ values ranging from -50 ‰ to -30 ‰ V-PDB (Schoell, 1980; Whiticar, 1999). However, these isotopic signatures should be considered indicative rather than definitive, as overlaps can occur due to secondary processes such as fractionation or mixing of gases from different origins (Mattavelli et al., 1983), especially in complex geological settings. The isotopic analysis of SMN soil gases reveals a distinctly biogenic origin, with all $\delta^{13}\text{C}-\text{CH}_4$ values below -60 ‰ V-PDB (Table 2). Fig. 4a illustrates the relationship between $\delta^{13}\text{C}-\text{CH}_4$ and $\delta^{13}\text{C}-\text{CO}_2$, contextualised within the genetic fields and isotopic processes defined by Milkov and Etiope (2018). The isotopic composition of soil gases from the SMN site falls within the CO_2 reduction (CR) field, indicating that CH_4 is primarily generated through microbial carbonate reduction in marine sediments. This pathway favours the production of ^{12}C -enriched CH_4 , which is consistent with the characteristics of CH_4 emissions in the area (Tassi et al., 2012). The $\delta^{13}\text{C}-\text{CO}_2$ values of the soil samples also provide further insights that point to other methane-related processes. While approximately half of the samples display $^{13}\text{C}/^{12}\text{C}$ ratio values typical of CO_2 sources linked to soil respiration and organic matter decomposition (e.g. -20 ‰ to -30 ‰ V-PDB; Amundson et al., 1998), others exhibit significantly depleted $\delta^{13}\text{C}-\text{CO}_2$ values (e.g., 23D: -52 ‰, 23E: -37 ‰, 23A: -39 ‰). Such highly negative values suggest an enhanced influence of methanotrophic activity, where the microbial oxidation of CH_4 results in the transfer of the $\delta^{13}\text{C}-\text{CH}_4$ signature to CO_2 through isotopic mass balance, ^{12}C being preferentially incorporated into the oxidised CO_2 . Although some degree of atmospheric

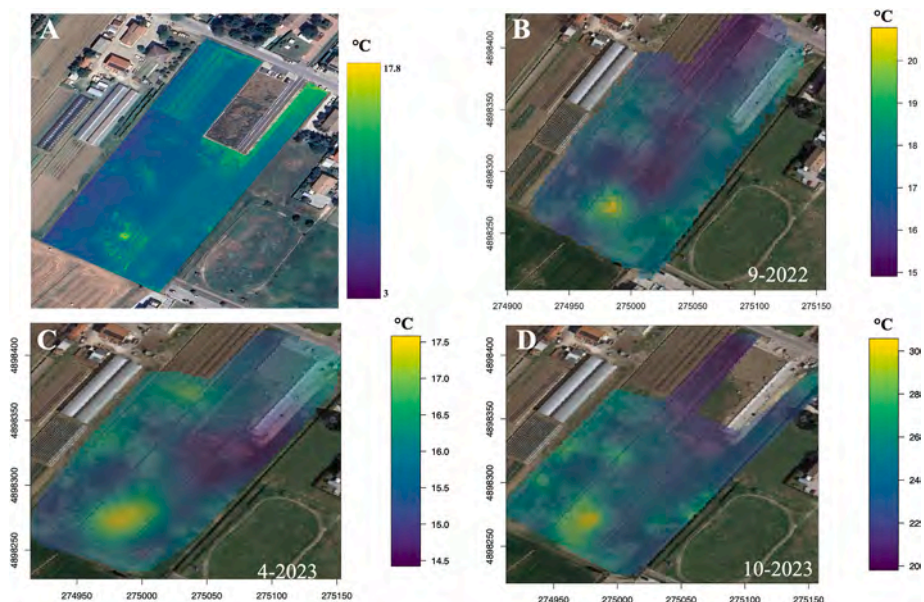


Fig. 5. Orthomosaic image captured by the drone with a thermal camera (a) and thermal maps generated using sGs interpolation from ground measurements (b, c, and d).

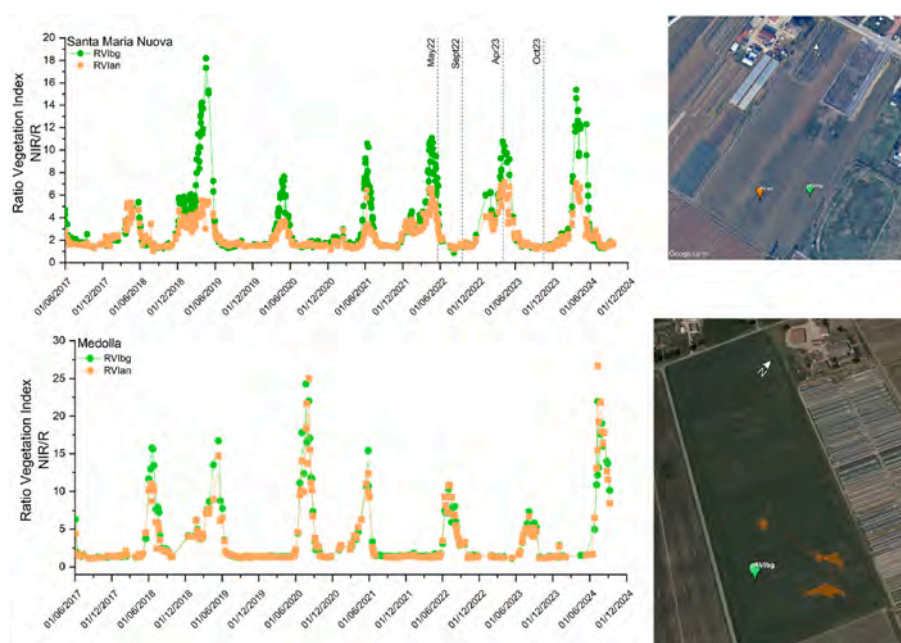


Fig. 6. Time series of the Ratio Vegetation Index (RVI) derived from Sentinel-2 data for the SMN site (upper panel) and Terre Calde di Medolla site (lower panel) over the 2017–2024 period. At each site, RVI was calculated both over vegetated background areas (RVI_{bg} , in green) and over zones affected by CH_4 seepage (RVI_{an} , in orange). The satellite images display the points from which the indices were derived. Dashed vertical lines in the SMN panel mark the dates of the four gas flux surveys conducted in May 2022, September 2022, April 2023, and October 2023. (For interpretation of the references to colour in this figure legend, the reader is referred to the Web version of this article.)

contamination may affect the $\delta^{13}C$ values in certain samples (particularly in sample 22A, which is characterised by low CO_2 concentrations and roughly atmospheric N_2 and O_2 values), the overall isotopic signatures remain consistently depleted in ^{13}C . This suggests that atmospheric dilution has a limited impact on the measured isotopic composition of both gases and does not significantly bias the interpretation of their origin. Fig. 4b further supports this interpretation by showing the relationship between $\delta^{13}C-CH_4$ and the CH_4/CO_2 ratio. The observed trend indicates that as CH_4/CO_2 decreases, $\delta^{13}C-CH_4$ becomes progressively enriched in ^{13}C . For comparison, Fig. 4b also includes gas data from the

Terre Calde di Medolla site, sourced from Capaccioni et al. (2015). Despite variations in sampling depth, these data exhibit a similar trend of increasing $\delta^{13}C-CH_4$ values with decreasing CH_4/CO_2 ratios. The extent of CH_4 oxidation, however, is likely influenced by several environmental factors, including oxygen availability, temperature, soil moisture, microbial community density, soil composition, land use, and vegetation cover (Shukla et al., 2013). This interpretation aligns with the general characteristics of gas reservoirs in the Padania Plain and the southern Po River Basin, where CH_4 is generated at relatively shallow depths (1.5–2 km) and lower temperatures (~ 50 °C) within the

Pliocene-Pleistocene sedimentary infill of the Apennine Chain foredeep (Martinelli et al., 2012; Ricci et al., 2023). These microbial gas accumulations contrast with the thermogenic CH₄ found in the Emilian sector of the Apennines, west of the study area, where gas emissions display a clear thermogenic signature associated with deeper and higher-temperature formations (Tassi et al., 2012). The geological cross-section in Fig. 7 (trace shown in Fig. 1b) reveals that the marine deposits of Pliocene to Pleistocene age beneath the study area are less than 0.5 km thick. These sediments, consisting of alluvial gravel and sand with interbedded clay, directly overlie Messinian clay-sand alternations, as documented in the Cannuzzuola I well log (available at www.vidempi.com). Given that microbial carbonate reduction typically occurs in shallow, organic-rich marine sediments, the Pliocene-Pleistocene layers represent a plausible domain for bacterial CH₄ generation. The underlying evaporitic sequence is considered an unlikely host for organic matter. Instead, a deeper gas source could be associated with the Marnoso-Arenacea turbidite formation, which lies at depths exceeding 1 km. However, CH₄ from this unit, as reported by Mattavelli et al. (1983), is of mixed biogenic and thermogenic origin and typically exhibits a heavier carbon isotopic signature than that observed in our samples. Moreover, the cross-section highlights two reverse faults intersecting the stratigraphic succession. These tectonic structures may act as preferential pathways for the upward migration of gas, supporting the hypothesis that fault-controlled permeability plays a key role in channelling the emissions observed at the surface.

5.2. Spatial and temporal evolution of ΦCH_4 and ΦCO_2

The spatial distribution maps of the CH₄ soil fluxes reveal a confined area, located south of the agricultural field, of significant anomaly consistently detected throughout the two-year surveys (Fig. 3). During both spring campaigns (May 2022 and April 2023), the main CH₄ anomaly was consistently accompanied by a secondary flux anomaly located slightly to the west, an additional feature that was absent in the autumn surveys. Notably, CH₄ fluxes measured in spring reached values up to two orders of magnitude higher than those recorded in autumn.

This recurring pattern suggests a potential seasonal control on CH₄ seepage. Various factors could drive this seasonality, with soil moisture playing a key role by influencing soil permeability and gas transport pathways. However, further targeted investigations are necessary to clarify the mechanisms underlying this seasonal variability. According to the Etiope and Klusman (2010) classification, high CH₄ microseepage is defined as fluxes greater than 50 mg m⁻² d⁻¹, medium microseepage ranges from 5 to 50 mg m⁻² d⁻¹, and low microseepage is from 0 to 5 mg m⁻² d⁻¹. At SMN, many CH₄ fluxes vastly exceeded the high microseepage range (Table 1), even when environmental factors inhibit the flux. The spatial distribution of ΦCO_2 mirrored that of ΦCH_4 (Fig. 3), consistent with both gases being produced and consumed by microbial activity. This pattern aligns with previous studies in the Terre Calde di Medolla area (Capaccioni et al., 2015), which documented a strong correlation between CH₄ and CO₂ fluxes at sites dominated by microbial gas generation and oxidation processes. Typical biogenic soil respiration fluxes of CO₂ in similar environments, in the absence of additional sources, generally reach several tens of g m⁻² d⁻¹ (Chiodini et al., 2008). In the anomalous spots of the study area, the observed ΦCO_2 values exceed these background levels, indicating a significant contribution from methanotrophy. To quantify the relative contribution of CH₄ oxidation and background soil respiration to total CO₂ flux, the distribution of September 2022 CO₂ flux values was modelled using a Gaussian Mixture Model (GMM), applying the Expectation-Maximisation (EM) algorithm to fit a finite model representing two normal populations of the empirical distribution. This statistical decomposition enabled the estimation of the mean and mixing fraction of each population (Fig. 8). The lower CO₂ flux population, which is the most common, represents background soil respiration and is observed across both areas with and without CH₄ anomalies. This population accounted for 69 % of the total flux, while the population associated with CH₄ oxidation contributed the remaining 31 %. The mean and standard deviation of these two components were used in a Monte Carlo simulation with 3000 iterations to estimate the mean flux and associated uncertainty for each population. The results indicated flux values of 143.2 ± 26.5 g CO₂ m⁻² d⁻¹ for the CH₄ oxidation

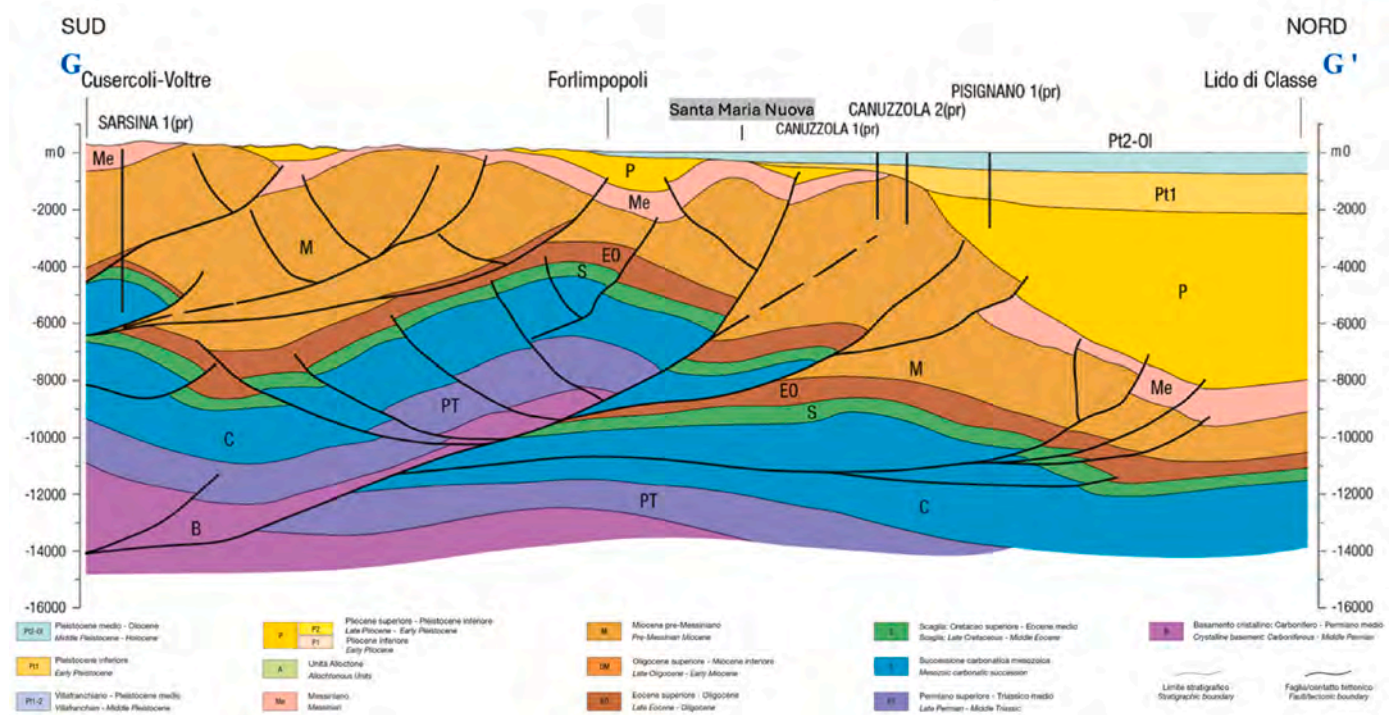


Fig. 7. The cross-section G-G', the trace of which is taken from the seismotectonic map in Fig. 1b (Emilia-Romagna Region, 2016), illustrates the geological setting of the subsurface of the study area, located between Forlimpopoli and the Cannuzzuola I well.

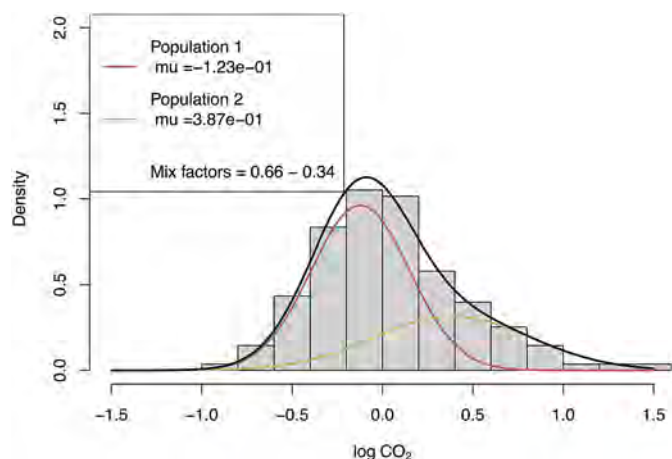


Fig. 8. The mixing plot for the September 2022 flux campaign was created using the logarithm of CO₂ fluxes. The plot illustrates the proportion of the two CO₂ mixing factors, along with the mean value (μ) for each population: soil respiration in red and methane oxidation in green. (For interpretation of the references to colour in this figure legend, the reader is referred to the Web version of this article.)

population and $36.7 \pm 2.7 \text{ g CO}_2 \text{ m}^{-2} \text{ d}^{-1}$ for the background soil respiration population.

5.3. Thermal anomaly and vegetation health assessment

A significant discrepancy in the recorded temperature ranges emerges between thermal maps derived from drone-based imaging and those obtained from ground-based measurements (Fig. 5). This is primarily due to the nature of the measurements since drone imaging captures the surface temperature, while the other maps represent soil temperature at a depth of 15 cm. Additionally, the thermal emissivity coefficient (ϵ) is uniformly applied to the entire acquisition, disregarding the presence of materials different from the soil (e.g., cement, metal from orchard fences). Despite the thermal maps not being directly comparable, this approach enables the identification of thermal anomalies while providing spatial continuity for the temperature parameter observed across various time intervals. The highest temperatures were consistently measured at and around the main CH₄ emission spot, even across time (Fig. S2), where the exothermic oxidation of CH₄ to CO₂ generates localised heating (Capaccioni et al., 2015). Seasonal variations in ground temperature and soil moisture modulate the extent and intensity of this thermal anomaly since these environmental factors influence gas mobility and microbial growth in the soil. Furthermore, the release of CH₄ and subsequent oxidation into CO₂ by methanotrophic bacteria affect plant health, often leading to a charred appearance and irregular, thinning growth near the gas leaks (Davis, 1977). These stress responses are further compounded by changes in nutrient cycling and microbial competition, which can reduce nitrogen availability essential for plant development (Karbin et al., 2015; Chang et al., 2024). The observed oxygen depletion in three interstitial gas soil samples (22B, 23D, 23E) also indicates that oxidative methane processes could impair root respiration. The adverse effects on vegetation are reflected in the RVI time series at SMN (Fig. 6), which shows consistently lower values at the anomaly spot compared to the surrounding areas. The seasonal RVI fluctuations (higher in spring and summer, lower in fall and winter) indicate regular vegetation cycles in unaffected regions. In contrast, the anomaly spot exhibits suppressed growth, reinforcing the hypothesis that CH₄ emissions negatively impact plant health. This difference in vegetation vitality is captured through satellite-derived spectral reflectance data. Typically, an RVI < 1 signals significant vegetation stress or sparse cover due to lower NIR reflectance relative to Red light (Richardson and Wiegand, 1977). However, despite expected distress

from gas seepage, the anomaly (RVI_{an}) remains above this threshold, likely due to the 10 m resolution of Sentinel-2, which averages localised effects over a broader area, thus diluting the visible impact on vegetation. Other factors may also influence RVI, including the phenological stage, where young or senescing plants exhibit different reflectance from mature vegetation (Kobayashi et al., 2018). Additionally, the crop rotation (i.e., barley cultivation in 2022 and fava bean in 2024) introduces species with distinct spectral characteristics due to differences in leaf structure and water content, further altering the RVI. Soil moisture and background reflectance are also essential; moist soils reduce NIR reflectance, while dry soils increase it, potentially lowering RVI values (Polivova and Brook, 2022). A direct comparison of the SMN and Medolla RVI time series enhances understanding of how vegetation responds to gas-related stress under various site conditions. At both sites, the anomaly RVI consistently shows lower values than the surrounding background RVI, indicating persistent reduction in vegetation vitality near the gas seepage areas. However, the RVI_{bg}–RVI_{an} gap is notably wider at SMN (especially evident during the growing seasons), suggesting more intense or sustained stress. In contrast, the Medolla site exhibits more robust vegetation growth overall, with higher and sharper RVI peaks, even at the anomaly location, implying either less severe environmental stress or more favourable baseline conditions. The more pronounced vegetation decline at SMN could be linked to chronic exposure to CH₄ emissions, whereas the stress at Medolla may be more episodic or buffered by local factors such as soil composition, land management, or microclimatic conditions.

6. Conclusions

The study investigated the spatial and temporal variability of CH₄ microseepage and associated ground heating phenomena at SMN site, in northern Italy. Seasonal gas flux monitoring revealed that methane emissions can vary by up to three orders of magnitude, with peak fluxes typically occurring in spring. The CH₄ seepage is attributed to microbial generation in shallow marine carbonate-rich sediments, consistent with other known seepage systems in the Po Plain. The observed ground heating, likely linked to exothermic methanotrophic oxidation, is associated with inhibited vegetation growth at the seepage site. Long-term satellite observations support the persistence of these effects over multiple years. Future studies could expand on these findings by incorporating vegetation stress indicators, such as chlorophyll content or spectral indices, to better quantify the impact of soil heating on plant health. Additionally, stable isotope analysis of plant tissues or rhizosphere gases could help refine the understanding of methane–biosphere interactions at these seepage sites.

CRedit authorship contribution statement

G. Capelli Ghioldi: Writing – original draft, Visualization, Validation, Resources, Methodology, Investigation, Formal analysis, Data curation, Conceptualization. **G. Tamburello:** Writing – original draft, Validation, Supervision, Software, Resources, Project administration, Methodology, Investigation, Formal analysis, Data curation, Conceptualization. **A. Sciarra:** Writing – review & editing, Validation, Resources, Methodology, Investigation. **D. Rouwet:** Writing – review & editing, Validation, Resources, Methodology, Investigation. **T. Ricci:** Writing – review & editing, Validation, Resources, Methodology, Investigation. **R. Civico:** Writing – review & editing, Validation, Resources, Methodology, Investigation. **F. Tassi:** Writing – review & editing, Validation, Supervision, Resources. **P. Severi:** Writing – review & editing, Resources, Methodology, Investigation. **M. Liuzzo:** Writing – review & editing, Validation, Resources, Methodology, Investigation. **M. Coltorti:** Writing – review & editing, Resources, Methodology, Investigation. **A.L. Rizzo:** Writing – review & editing, Validation.

Declaration of competing interest

The authors declare that they have no known competing financial interests or personal relationships that could have appeared to influence the work reported in this paper.

Acknowledgements

This research was carried out in the framework of the "Rete Multi-parametrica" (D.P. n.74/2020) and Progetto DL50 "Centro Italia" - Ricostruzione (D.P. 76/2020) projects, of the Istituto Nazionale di Geofisica e Vulcanologia. The researchers sincerely thank Matteo, the owner of the agricultural field, for his constant availability and support in allowing us to conduct our research. We sincerely thank the Editor and the reviewers for their valuable corrections and insightful comments, which significantly improved the quality of this manuscript.

Appendix A. Supplementary data

Supplementary data to this article can be found online at <https://doi.org/10.1016/j.apgeochem.2025.106565>. Raw data analysed in this study are provided via figshare (<https://doi.org/10.6084/m9.figshare.30102466.v1>).

Data availability

Data will be made available on request.

References

- Abrams, M.A., 2005. Significance of hydrocarbon seepage relative to petroleum generation and entrapment. *Mar. Pet. Geol.* 22, 457–477.
- Amundson, R., Stern, L., Baisden, T., Wang, Y., 1998. The isotopic composition of soil and soil-respired CO₂. *Geoderma* 82 (Issues 1–3), 83–114. [https://doi.org/10.1016/S0016-7061\(97\)00098-0](https://doi.org/10.1016/S0016-7061(97)00098-0).
- Boccaletti, M., Elter, P., Guazzone, G., 1971. Plate tectonics models for the development of the western Alps and northern Apennines. *Nature* 234, 108–111.
- Bonzi, L., Ferrari, V., Martinelli, G., Norelli, E., Severi, P., 2017. Unusual geological phenomena in the Emilia-Romagna plain (Italy): gas emissions from wells and the ground, hot water wells, geomorphological variations. A review and an update of documented reports. *Boll. Geofis. Teor. Appl.* 58 (2), 87–102. <https://doi.org/10.4430/bgta0193>.
- Boothroyd, I.M., Almond, S., Qassim, S.M., Worrall, F., Davies, R.J., 2016. Fugitive emissions of methane from abandoned, decommissioned oil and gas wells. *Sci. Total Environ.* 547, 461–469. <https://doi.org/10.1016/j.scitotenv.2015.12.096>.
- Capaccioni, B., Tassi, F., Cremonini, S., Sciarra, A., Vaselli, O., 2015. Ground heating and methane oxidation processes at shallow depth in Terre Calde di Medolla (Italy): observations and conceptual model. *J. Geophys. Res. Solid Earth* 120, 3048–3064. <https://doi.org/10.1002/2014JB011635>.
- Capozzi, R., Picotti, V., 2002a. Fluid migration and origin of a mud volcano in the Northern Apennines (Italy): the role of deeply rooted normal faults. *Terra Nova* 14 (5), 363–370. <https://doi.org/10.1046/j.1365-3121.2002.00430.x>.
- Capozzi, R., Picotti, V., 2002b. Pliocene sequence stratigraphy, climatic trends and sapropel formation in the Northern Apennines (Italy). *Palaeogeogr. Palaeoclimatol. Palaeoecol.* 190, 349–371. [https://doi.org/10.1016/S0031-0182\(02\)00614-4](https://doi.org/10.1016/S0031-0182(02)00614-4), 2003.
- Capozzi, R., Picotti, V., 2010. Spontaneous fluid emissions in the Northern Apennines: Geochemistry, structures and implications for the petroleum system. *Geol. Soc. Spec. Publ.* 348 (7), 115–135. <https://doi.org/10.1144/SP348>.
- Cardellini, C., Chiodini, G., Frondini, F., 2003. Application of stochastic simulation to CO₂ flux from soil: mapping and quantification of gas release. *J. Geophys. Res.* 108, 2425. <https://doi.org/10.1029/2002JB002165>.
- Chang, S., Zhou, A., Hua, Z., Meng, H., Zhu, F., Li, S. and He, H. 2024. Microplastics alter soil carbon cycling: Effects on carbon storage, CO₂ and CH₄ emission and microbial community. *Cambridge Prisms: Plastics*, 2, e5, 1–12. <https://doi.org/10.1017/pic.2024.5>.
- Chiodini, G., Cioni, R., Guidi, M., Raco, B., Marini, L., 1998. Soil CO₂ flux measurements in volcanic and geothermal areas. *Appl. Geochem.* 13, 543–552. [https://doi.org/10.1016/S0883-2927\(97\)00076-0](https://doi.org/10.1016/S0883-2927(97)00076-0).
- Chiodini, G., Caliro, S., Cardellini, C., Avino, R., Granieri, D., Schmidt, A., 2008. Carbon isotopic composition of soil CO₂ efflux, a powerful method to discriminate different sources feeding soil CO₂ degassing in volcanic-hydrothermal areas. *Earth Planet Sci. Lett.* 274, 372–379. <https://doi.org/10.1016/j.epsl.2008.07.051>.
- Davis, S.H., 1977. The effect of natural gas on trees and other vegetation. *Arboric. Urban For.* 3 (8), 153–154. <https://doi.org/10.48044/jauf.1977.039>.
- Deutsch, C.V., Journel, A.G., 1998. *GSLIB: Geostatistical Software Library and Users Guide*. Oxford University Press, New York, p. 369.
- EMEP-EEA, 2023. Geological seepage – B1109. Natural sources. EMEP/EEA Air Pollutant Emission Inventory Guidebook – 2023 – Chapter 11. Technical Guidance to Prepare National Emission Inventories. EEA Technical Report N° 6/2023. European Environment Agency, Copenhagen. <https://doi.org/10.2800/795737>.
- Emilia-Romagna, Regione, Agip, E.N.I., 1998. *Riserve idriche sotterranee della Regione Emilia-Romagna*. A cura di G. Di Dio. S. EL.CA., Firenze, p. 120.
- Etiopie, G., 1999. Subsoil CO₂ and CH₄ and their advective transfer from faulted grassland to the atmosphere. *J. Geophys. Res.* 104 (D14). <https://doi.org/10.1029/1999JD900299>, 16,889.
- Etiopie, G., 2009. Natural emissions of methane from geological seepage in Europe. *Atmos. Environ.* 43, 1430–1443. <https://doi.org/10.1016/j.atmosenv.2008.03.014>.
- Etiopie, G., Klusman, R.W., 2010. Methane microseepage in drylands: soil is not always a CH₄ sink. *J. Integr. Environ. Sci.* 7 (Suppl. 1), 31–38. <https://doi.org/10.1080/19438151003621359>.
- Etiopie, G., Fridriksson, T., Italiano, F., Winiwarter, W., Theloke, J., 2007. Natural emissions of methane from geothermal and volcanic sources in Europe. *J. Volcanol. Geoth. Res.* 165, 76–86. <https://doi.org/10.1016/j.jvolgeores.2007.04.014>.
- IPCC, 2021. In: Masson-Delmotte, V., Zhai, P., Pirani, A., Connors, S.L., Péan, C., Berger, S., Caud, N., Chen, Y., Goldfarb, L., Gomis, M.I., Huang, M., Leitzell, K., Lonnoy, E., Matthews, J.B.R., Maycock, T.K., Waterfield, T., Yelekçi, O., Yu, R., Zhou, B. (Eds.), *Climate Change 2021: the Physical Science Basis*. Contribution of Working Group I to the Sixth Assessment Report of the Intergovernmental Panel on Climate Change. Cambridge University Press, Cambridge, United Kingdom and New York, NY, USA, p. 2391. <https://doi.org/10.1017/9781009157896>.
- ISPRA, 2009. *Note illustrative della Carta Geologica d'Italia Foglio n. 255 Cesena e Folli 240-241 Forlì – Cervia*, 2005.
- Karbin, S., Guillet, C., Kammann, C.I., Niklaus, P.A., 2015. Effects of long-term CO₂ enrichment on soil-atmosphere CH₄ fluxes and the spatial micro-distribution of methanotrophic bacteria. *PLoS one* 10 (7), e0131665. <https://doi.org/10.1371/journal.pone.0131665>.
- Klusman, R.W., 1993. *Soil Gas and Related Methods for Natural Resource Exploration*. J. Wiley & Sons, Chichester, U.K, p. 483.
- Kobayashi, H., Nagai, S., Kim, Y., Yang, W., Ikeda, K., Ikawa, H., Nagano, H., Suzuki, R., 2018. In Situ observations reveal how spectral reflectance responds to growing season phenology of an open evergreen forest in Alaska. *Remote Sens.* 10, 1071. <https://doi.org/10.3390/rs10071071>.
- Laubmeyer, G., 1933. *A New Geophysical Prospecting Method, Especially for Deposits of Hydrocarbons: Petrol*, vol. 29, p. 14. London.
- Marroni, M., Molli, G., Montanini, A., Ottria, G., Pandolfi, L., Tribuzio, R., 2002. The external Ligurian units (Northern Apennine, Italy): from rifting to convergence of a fossil ocean-continent transition zone. *Ofoliti* 27, 119–131. <https://doi.org/10.4454/ofoliti.v27i2.182>.
- Martinelli, G., Cremonini, S., Samonati, E., 2012. Geological and geochemical setting of natural hydrocarbon emissions in Italy. In: Al-Megren, H. (Ed.), *Advances in Natural Gas Technology*. InTech, London.
- Mattavelli, L., Ricchiuto, T., Grignani, D., Schoell, M., 1983. Geochemistry and habitat of natural gases in Po basin, Northern Italy. *AAPG Bull.* 67 (12), 2239–2254. <https://doi.org/10.1306/AD46094F-16F7-11D7-8645000102C1865D>.
- Milkov, A.V., Etiopie, G., 2018. Revised genetic diagrams for natural gases based on a global dataset of >20,000 samples. *Org. Geochem.* 125, 109–120. <https://doi.org/10.1016/j.orggeochem.2018.09.002>. ISSN 0146-6380.
- Pearson, R.L., Miller, L.D., 1972. Remote mapping of standing crop biomass for estimation of the productivity of the shortgrass prairie, Pawnee National Grasslands, Colorado. *Proc. 8th Int. Sympos. Rem. Sens. Environ.* II, 1355–1379.
- Polivova, M., Brook, A., 2022. Detailed investigation of spectral vegetation indices for fine field-scale phenotyping. *Vegetation Index Dynam. IntechOpen Crossref*. <https://doi.org/10.5772/intechopen.96882>.
- Ricci, A., Cremonini, S., Severi, P., Tassi, F., Vaselli, O., Rizzo, A.L., Caracausi, A., Grassa, F., Fiebig, J., Capaccioni, B., 2023. Sources and migration pathways of methane and light hydrocarbons in the subsurface of the Southern Po River Basin (Northern Italy). *Mar. Petrol. Geol.* 147. <https://doi.org/10.1016/j.marpetgeo.2022.105981>.
- Richardson, A.J., Wiegand, C.L., 1977. Distinguishing vegetation from soil background information. *Photogramm. Eng. Rem. Sens.* 43 (12), 1541–1552.
- Schoell, M., 1980. The hydrogen and carbon isotopic composition of methane from natural gases of various origins. *Geochem. Cosmochim. Acta* 44, 649–661. [https://doi.org/10.1016/0016-7037\(80\)90155-6](https://doi.org/10.1016/0016-7037(80)90155-6).
- Schout, G., Hartog, N., Hassanizadeh, S.M., Helmig, R., Griffioen, J., 2020. Impact of groundwater flow on methane gas migration and retention in unconsolidated aquifers. *J. Contam. Hydrol.* 230. <https://doi.org/10.1016/j.jconhyd.2020.103619>.
- Sciarra, A., Cantucci, B., Buttinelli, M., Galli, G., Nazzari, M., Pizzino, L., Quattrocchi, F., 2012. Soil-gas survey of liquefaction and collapsed caves during the Emilia seismic sequence. *Ann. Geophys.* 55 (4). <https://doi.org/10.4401/ag-6122>.
- Sciarra, A., Cantucci, B., Coltorti, M., 2017. Learning from soil gas change and isotopic signatures during the 2012 Emilia seismic sequence. *Sci. Rep.* 7 (1). <https://doi.org/10.1038/s41598-017-14500-y>.
- Sciarra, A., Cantucci, B., Sapia, V., De Ritis, R., Ricci, T., Civico, R., Galli, G., Cinti, D., Coltorti, M., 2021. Geochemical and geolectrical characterization of the Terre Calde di Medolla (Emilia-Romagna, northern Italy) and relations with 2012 seismic sequence. *J. Geochem. Explor.* 221, 106678. <https://doi.org/10.1016/j.gexplo.2020.106678>.
- Severi, P., Bonzi, L., 2014. *Esperienze e prospettive nel monitoraggio delle acque sotterranee*. In: Farina, M., Marcaccio, M., Zavatti (Eds.), *Il Contributo dell'Emilia-Romagna*. Cured, A. Chapter 2. Pitagora Editrice Bologna.
- Shukla, P.N., Pandey, K.D., Mishra, V.K., 2013. Environmental determinants of soil methane oxidation and methanotrophs. *Critical Reviews in Environmental Science*

- and Technology 43 (18), 1945–2011. <https://doi.org/10.1080/10643389.2012.672053>.
- Tassi, F., Bonini, M., Montegrossi, G., Capecchiacci, F., Capaccioni, B., Vaselli, O., 2012. Origin of light hydrocarbons in gases from mud volcanoes and CH₄-rich emissions. *Chem. Geol.* 294–295, 113–126. <https://doi.org/10.1016/j.chemgeo.2011.12.004>. ISSN 0009-2541.
- Tassi, F., Venturi, S., Cabassi, J., Capecchiacci, F., Nisi, B., Vaselli, O., 2015. Volatile organic compounds (VOCs) in soil gases from Solfatara crater (Campi Flegrei, southern Italy): geogenic source(s) vs. biogeochemical processes. *Appl. Geochem.* 56, 37–49. <https://doi.org/10.1016/j.apgeochem.2015.02.005>.
- Tedesco, S.A., 1995. *Surface Geochemistry in Petroleum Exploration*. Chapman & Hall, New York, p. 206.
- Tucker, C.J., 1979. Red and photographic infrared linear combinations for monitoring vegetation. *Rem. Sens. Environ.* 8, 127–150. [https://doi.org/10.1016/0034-4257\(79\)90013-0](https://doi.org/10.1016/0034-4257(79)90013-0).
- Whiticar, M.J., 1999. Carbon and hydrogen isotope systematics of bacterial formation and oxidation of methane. *Chem. Geol.* 161, 291–314. [https://doi.org/10.1016/S0009-2541\(99\)00092-3](https://doi.org/10.1016/S0009-2541(99)00092-3).